

Expression of the angular dependence of the quantum efficiency for a thin multi-alkali photocathode and its optical properties

Kodai Matsuoka

Kobayashi-Maskawa Institute, Nagoya University, Nagoya 464-8602, Japan

**E-mail: matsuoka@hepl.phys.nagoya-u.ac.jp*

.....
The dependence of the quantum efficiency on the angle and polarization of the incident photon needs to be formulated for a precise description of the response of photomultiplier tubes. A simplified one step model of photoelectron emission was derived from Spicer's three step model, and it enabled the formulation of the dependence of the quantum efficiency in the visible range for thin multi-alkali (NaKSbCs) photocathodes. The expression of the quantum efficiency was proved by a measurement of the photocurrent for linearly polarized light at various incident angles. Meanwhile the measurement revealed the complex refractive indices and thicknesses both of the stratified photocathode and antireflection coating. It is indicated that the angular dependence of the quantum efficiency is dictated by the optical properties of the photocathode, which are discussed in detail on the basis of the obtained parameters.
.....

Subject Index H02, H15

1. Introduction

The photocathode is a key component of photomultiplier tubes (PMTs). It dominates the PMT performance in terms of the sensitivity to photons. As PMTs are used in a variety of fields, photocathode properties are major subjects of research. One of the most important properties is the efficiency of photoelectron emission, or the quantum efficiency (QE). The QE depends not only on the wavelength but also on the incident angle and polarization of the light. Those dependences are of great interest especially for Cherenkov detectors because the Cherenkov light is emitted along the definite Cherenkov angle and is naturally 100% linearly polarized [1, 2]. Rigorous expression of the dependences of the QE is demanded to precisely estimate or calibrate the detector performance [3–6]. Furthermore detailed understanding of the QE could help to find a recipe for enhancement of the QE.

The process of the photoelectron emission can be described by Spicer's three-step model [7]: (1) photoexcitation of an electron in the photocathode, (2) transport of the excited electron to the vacuum surface and (3) escape of the electron over the surface barrier into the vacuum. Therefore the QE is dictated by the optical properties of the PMT, the physical properties of the photocathode material such as the band structure and the electron scattering mechanisms during transportation, and the quality of the photocathode such as the surface characteristics. Each of these has to be well described for expression of the dependence of the QE. Some theoretical expressions or practical models of photoelectron emission were

proposed for metal [8–10] and semiconductor [7, 11, 12] under assumption of infinite thickness of the photocathode, where it was not necessary to treat the optical properties of the photocathode in detail because the photon absorption follows a simple exponential function of the depth (Lambert-Beer law). For thin photocathodes, which are widely used for PMTs, however, the optical properties are of more complication, and there are yet no expressions of photoelectron emission which have been theoretically or experimentally verified.

The optical properties can be expressed by means of the complex refractive index and the thickness of the photocathode. These parameters can be derived from the standard techniques of reflectance measurement at various angles or of ellipsometry. Such measurements were reported in Refs. [13–19] for various photocathode types but only at a few wavelengths. Measurements over the whole visible range were done in Refs. [20–23] for bi/multi-alkali photocathodes. Among them Refs. [17, 18] made comparison between the measured angular dependence of the photocurrent and the predicted one of the absorptance from the measured index and thickness of the photocathode, and found some unexplained discrepancies. Another attempt to derive the photocathode index and thickness can be made by photocurrent measurement at various angles. This method was adopted by Ref. [24], but the theoretical function he applied did not fit the data precisely in terms of the angular dependence of the photocurrent. A discrepancy on the angular dependence was also found between the measurements of the photocurrent and the absorptance by Ref. [25]. The biggest concern in those comparisons is that some interpretations are needed to connect the photocurrent to the optical absorptance. Hence the dependence of the QE on the angle and polarization is yet to be investigated. In addition available data of photocathode indices are not satisfactory for the whole visible range.

In this paper a simplified expression of the QE for thin photocathodes is proposed based on Spicer’s three step model. It is verified by the measurement of the dependence of the QE on the angle and polarization. The dependence of the QE was examined directly by the photocurrent measurement for a thin multi-alkali (NaKSbCs) photocathode of transmission mode, fabricated in a square-shaped micro-channel-plate (MCP) PMT R10754-07-M16(N) [26] made by HAMAMATSU PHOTONICS K.K. The photocurrent was measured at wavelengths from 320 to 680 nm and at incident angles from 0 to 80° both for s- and p-polarizations. It has to be noted that this PMT has a confidential antireflection coating, of which optical properties are totally unknown. Hence the optical parameters of the stratified photocathode and antireflection coating are derived at the same time in this work. Based on the measured parameters, in the latter part of this paper, the optical properties of the photocathode are discussed in connection with effects on the QE.

2. Expression of the quantum efficiency

In this section the simplified expression of the QE is derived for thin multi-alkali photocathodes. Based on the three-step model, the QE can be factorized into the probabilities A_{pc} , $P_{\text{transport}}$ and P_{escape} , where A_{pc} is the absorptance of the photocathode or the fraction of the absorbed light intensity to the incident one, and $P_{\text{transport}}$ and P_{escape} are the probabilities that the electron reaches the vacuum surface and escapes into the vacuum, respectively. These three factors are functions of the photon wavelength because $P_{\text{transport}}$ and P_{escape} depend on the energy of the electron, which is determined by the photoexcitation process being subject to the energy of the absorbed photon. $P_{\text{transport}}$ and P_{escape} also depend on the

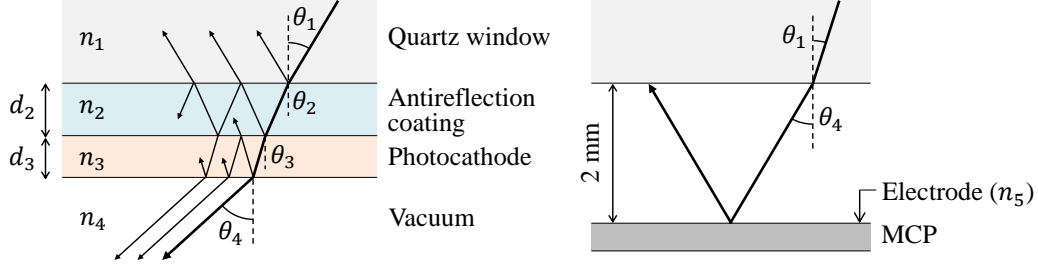


Fig. 1: (Left) Diagram of light passing through a double thin layer of the antireflection coating and the photocathode. Multiple reflections in the thin layers are also drawn to some extent. (Right) Diagram of light transmitted through the photocathode and reflected on the MCP electrode.

depth z where the photon is absorbed due to a loss of the electron energy during transportation. That demands a differential function of A_{pc} , represented as $A'_{\text{pc}}(z)$, which describes the absorption distribution along z . Therefore the QE at a wavelength λ is expressed in the form

$$QE(\lambda) = \int_0^d A'_{\text{pc}}(z, \lambda) P_{\text{transport}}(z, \lambda) P_{\text{escape}}(z, \lambda) dz, \quad (1)$$

where d is the thickness of the photocathode. It also has to be expressed as a function of the angle θ and the polarization ϵ ($=$ s or p) of the incident light. In the following, each factor of this equation is described by elementary functions with several parameters based on theories.

2.1. Optical model

The absorptance A_{pc} and its derivation A'_{pc} are fully described by the optics. A specific configuration of the PMT shown in Fig. 1 is considered here¹: the light passes from the quartz window (layer 1 with refractive index n_1) through a double thin layer of the antireflection coating (layer 2 with n_2) and the photocathode (layer 3 with n_3) into the vacuum (layer 4 with $n_4 = 1$). The amplitude reflection and transmission coefficients at the interface from layer i to $j = i + 1$ (r_{ij} and t_{ij} , respectively, and $i = 1, 2, 3$) are described by Fresnel equations:

$$\begin{aligned} r_{ij} &= \frac{n_i \cos \theta_i - n_j \cos \theta_j}{n_i \cos \theta_i + n_j \cos \theta_j}, & t_{ij} &= \frac{2n_i \cos \theta_i}{n_i \cos \theta_i + n_j \cos \theta_j} & (\text{s-polarization}), \\ r_{ij} &= \frac{n_j \cos \theta_i - n_i \cos \theta_j}{n_j \cos \theta_i + n_i \cos \theta_j}, & t_{ij} &= \frac{2n_i \cos \theta_i}{n_j \cos \theta_i + n_i \cos \theta_j} & (\text{p-polarization}), \end{aligned} \quad (2)$$

where θ_i (θ_j) is the angle between the incident (refracted) light and the normal of the interface, which follows Snell's law:

$$n_i \sin \theta_i = n_j \sin \theta_j. \quad (3)$$

¹ In most cases light comes from the outside of the window, and one should also consider the reflection and refraction at the outer surface of the window.

It should be noted that Eq. (3) holds for any combination of i and $j > i$. When layer l absorbs the light or has stimulated emission, n_l and θ_l are complex numbers. Taking into account the multiple reflections on both surfaces of the photocathode, the amplitude reflection and transmission coefficients for the photocathode layer (\hat{r}_3 and \hat{t}_3 , respectively) are described using Eq. (2) as follows:

$$\begin{aligned}\hat{r}_3 &= r_{23} + t_{23}r_{34}t_{32}e^{i\delta_3} \sum_{m=0}^{\infty} (r_{32}r_{34}e^{i\delta_3})^m = \frac{r_{23} + r_{34}e^{i\delta_3}}{1 + r_{34}r_{23}e^{i\delta_3}}, \\ \hat{t}_3 &= t_{23}t_{34}e^{i\delta_3/2} \sum_{m=0}^{\infty} (r_{34}r_{32}e^{i\delta_3})^m = \frac{t_{23}t_{34}e^{i\delta_3/2}}{1 + r_{34}r_{23}e^{i\delta_3}},\end{aligned}\tag{4}$$

and similarly for the double layer:

$$\hat{r}_{2+3} = \frac{r_{12} + \hat{r}_3 e^{i\delta_2}}{1 + \hat{r}_3 r_{12} e^{i\delta_2}}, \quad \hat{t}_{2+3} = \frac{t_{12} \hat{t}_3 e^{i\delta_2/2}}{1 + \hat{r}_3 r_{12} e^{i\delta_2}},\tag{5}$$

where

$$\delta_l = \frac{4\pi d_l n_l}{\lambda_0} \cos \theta_l \quad (l = 2, 3)\tag{6}$$

is the phase difference, d_l is the thickness of layer l and λ_0 is the wavelength of the light in the vacuum. The reflectance R_{2+3} and transmittance T_{2+3} of the double layer are related to the coefficients:

$$R_{2+3} = |\hat{r}_{2+3}|^2,\tag{7}$$

$$T_{2+3} = \begin{cases} \frac{\text{Re}(n_4 \cos \theta_4)}{\text{Re}(n_1 \cos \theta_1)} |\hat{t}_{2+3}|^2 & \text{(s-polarization)} \\ \frac{\text{Re}(n_4 \cos \theta_4^*)}{\text{Re}(n_1 \cos \theta_1^*)} |\hat{t}_{2+3}|^2 & \text{(p-polarization)} \end{cases}\tag{8}$$

where θ^* denotes the complex conjugate of θ (although θ_1 and θ_4 are real in this case) and $\text{Re}(x)$ denotes the real part of x . Equation (7) is the base of the reflectance measurement for estimation of the photocathode index and thickness mentioned in Sec. 1. On the other hand the photocurrent measurement is associated with the absorptance of the double layer A_{2+3} , which has the relation:

$$R_{2+3} + T_{2+3} + A_{2+3} = 1.\tag{9}$$

If there is no absorption in the antireflection coating, A_{2+3} is equal to the absorptance of the photocathode A_3 .

An example of R_{2+3} , T_{2+3} and A_{2+3} as a function of θ_1 is shown in Fig. 2 for a given set of parameters. For s(p)-polarization A_{2+3} increases (decreases) along with the incident angle from 0° because at the photocathode-vacuum interface the reflection increases (decreases) and the transmission to the vacuum decreases (increases); Accordingly T_{2+3} decreases (increases) and falls down to zero at the total reflection angle for the photocathode-vacuum interface. The incident angle θ_1 corresponding to the total reflection angle is determined by the indices of quartz and vacuum according to Eq. (3). It ranges from 42.4° at 320 nm to 43.4° at 660 nm, where the quartz index varies from 1.48 to 1.46. Nearly at that angle A_{2+3} peaks for s-polarization and drops steeply for p-polarization. A_{2+3} for p-polarization then peaks and R_{2+3} drops to nearly zero. The angle of the minimum R_{2+3} is 57.1° , which is slightly

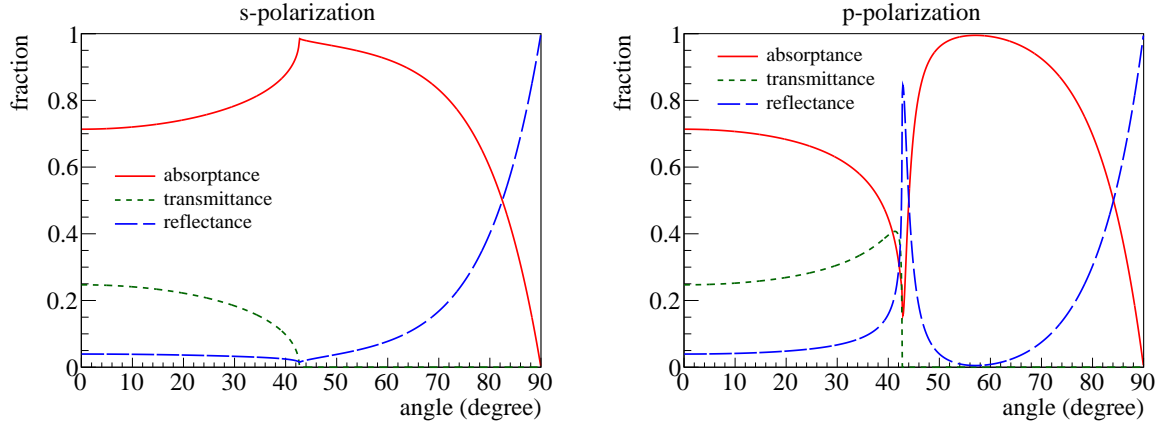


Fig. 2: Reflectance R_{2+3} , transmittance T_{2+3} and absorptance A_{2+3} of the double layer of the antireflection coating ($n_2 = 2.1$ and $d_2 = 30$ nm) and the photocathode ($n_3 = 2.3 + 3.3i$ and $d_3 = 10$ nm) at a wavelength $\lambda_0 = 360$ nm for s-polarization (left) and p-polarization (right). The indices of quartz and vacuum are $n_1 = 1.475$ at 360 nm and $n_4 = 1$.

different from Brewster's angle of $\arctan(n_2/n_1) = 54.9^\circ$ for the first interface between the window and the antireflection coating due to the reflections from the other interfaces. When the angle gets close to 90° the reflection at the first interface becomes dominant and thus A_{2+3} declines.

For the sake of precise expression of the absorptances of both stratified layers, the exact expression recently derived [27] is applied in this work. Namely the amount of light absorbed per unit length at a depth z from the surface of each layer $l(= 2, 3)$ ($z = 0$ on the light incident surface) is given as

$$A'_l(z) = a_l |v_l|^2 e^{-2z\text{Im}(\tilde{\nu}_l)} + a_l |w_l|^2 e^{2z\text{Im}(\tilde{\nu}_l)} + b_l v_l w_l^* e^{2iz\text{Re}(\tilde{\nu}_l)} + b_l v_l^* w_l e^{-2iz\text{Re}(\tilde{\nu}_l)}, \quad (10)$$

$$a_l = b_l = \frac{\text{Im}(\tilde{\nu}_l n_l \cos \theta_l)}{\text{Re}(n_1 \cos \theta_1)} \quad (\text{s-polarization})$$

$$a_l = \frac{2\text{Im}(\tilde{\nu}_l)\text{Re}(n_l \cos \theta_l^*)}{\text{Re}(n_1 \cos \theta_1^*)}, \quad b_l = -\frac{2\text{Re}(\tilde{\nu}_l)\text{Im}(n_l \cos \theta_l^*)}{\text{Re}(n_1 \cos \theta_1^*)} \quad (\text{p-polarization})$$

where $\text{Im}(x)$ denotes the imaginary part of x , $\tilde{\nu}_l$ is the z -component of the wavenumber in layer l , and v_l (w_l) is the amplitude of the wave heading forward (backward) on the layer l side of the interface between $l-1$ and l :

$$\tilde{\nu}_l = \frac{2\pi n_l}{\lambda_0} \cos \theta_l, \quad (11)$$

$$v_l = v_{l-1} e^{i\delta_{l-1}/2} t_{l-1,l} + w_l r_{l,l-1}, \quad (12)$$

$$w_l = w_{l+1} t_{l+1,l} e^{i\delta_l/2} + v_l r_{l,l+1} e^{i\delta_l}.$$

In the case of four layers considered,

$$\begin{aligned}
v_1 &= 1, & w_1 &= r_{12}, \\
v_2 &= \frac{(1 - r_{32}r_{34}e^{i\delta_3})t_{12}}{1 - r_{21}r_{23}e^{i\delta_2} - r_{32}r_{34}e^{i\delta_3} - r_{21}r_{34}e^{i(\delta_2+\delta_3)}}, & w_2 &= \frac{r_{23} + r_{34}e^{i\delta_3}}{1 - r_{32}r_{34}e^{i\delta_3}}e^{i\delta_2}v_2, \\
v_3 &= \frac{t_{23}e^{i\delta_2/2}}{1 - r_{32}r_{34}e^{i\delta_3}}v_2, & w_3 &= r_{34}e^{i\delta_3}v_3, \\
v_4 &= t_{34}, & w_4 &= 0.
\end{aligned} \tag{13}$$

The absorptance of layer l is given by integrating Eq. (10) over the thickness:

$$A_l = \int_0^{d_l} A'_l(z)dz. \tag{14}$$

It is also necessary to consider the transmitted light into the vacuum, which is then reflected on the MCP electrode back to the photocathode as shown in Fig. 1 (right). Hereafter the illumination from the window/vacuum side is called front/back-illumination. The back-illumination needs to be taken into account only below the total reflection angle for the photocathode-vacuum interface. The gap spacing between the photocathode and the MCP is 2 mm, and the back-illumination hits the photocathode at a different position from the front-illumination depending on the incident angle. The reflectance R_{el} of the electrode with refractive index n_5 is calculated using Eq. (2),

$$R_{\text{el}} = |r_{45}|^2. \tag{15}$$

The MCP has micro pores of 10 μm diameter and the open area ratio (\mathcal{R}_{OA}) is about 60%. Hence the fraction of the reflected light accounts for $(1 - \mathcal{R}_{\text{OA}})R_{\text{el}}$. The absorptance of each layer for the back-illumination $A_{\bar{l}}$ and its derivation $A'_{\bar{l}}(z)$ are given in the same manner as described above by reversing the order of the layers (namely $\bar{l} = \bar{1}, \bar{2}, \bar{3}, \bar{4}$ for the vacuum, photocathode, antireflection coating and window, respectively; and the indices $n_{\bar{l}}$ and thicknesses $d_{\bar{l}}$ should be defined correspondingly) and using θ_4 as the incident angle. The sum of the front- and back-illuminations is the total absorption of the photocathode,

$$A_{\text{pc}} = A_3 + T_{2+3}(1 - \mathcal{R}_{\text{OA}})R_{\text{el}}A_{\bar{2}}. \tag{16}$$

Subsequent reflections of the back-illumination in the vacuum layer are omitted in this work because they should have little contribution to A_{pc} .

2.2. Dispersion model

In order to describe dispersion functions of refractive indices, the following two models and an empirical equation are applied in this work.

The one for the photocathode and the antireflection coating is the Lorentz dispersion model [28], which represents dielectric response of inter-band transitions by the classical damped harmonic oscillator. As Ref. [20] infers that the photon absorption in NaKSbCs is probably of direct transition, the Lorentz model is expected to describe the dispersion well. In this model, the complex dielectric function of the frequency ω can be expressed as

$$\varepsilon(\omega) = \varepsilon_{\infty} + \frac{(\varepsilon_s - \varepsilon_{\infty})\omega_t^2}{\omega_t^2 - \omega^2 - i\Gamma_0\omega}, \tag{17}$$

where ε_{∞} is the high frequency limit of ε , $\varepsilon_s = \varepsilon_{\infty} + \omega_p^2/\omega_t^2$ is the static dielectric function at $\omega = 0$, ω_p is the plasma frequency, ω_t is the resonant frequency of the oscillator corresponding

to the absorption peak, and Γ_0 is the damping factor corresponding to the full width at half maximum of the peak. The real and imaginary parts of ε are described as follows:

$$\text{Re}(\varepsilon) = 1 + \frac{(\varepsilon_s - 1)\omega_t^2 (\omega_t^2 - \omega^2)}{(\omega_t^2 - \omega^2)^2 + \Gamma_0^2 \omega^2}, \quad \text{Im}(\varepsilon) = \frac{(\varepsilon_s - 1)\omega_t^2 \Gamma_0 \omega}{(\omega_t^2 - \omega^2)^2 + \Gamma_0^2 \omega^2}. \quad (18)$$

Here ε_∞ is fixed to 1 as in general material. The complex refractive index ($n + ik$) as a function of $\lambda (= 2\pi c/\omega)$ is derived as follows:

$$n(\lambda) = \sqrt{\frac{\text{Re}(\varepsilon) + |\varepsilon|}{2}}, \quad k(\lambda) = \sqrt{\frac{-\text{Re}(\varepsilon) + |\varepsilon|}{2}}. \quad (19)$$

The other dispersion model for the electrode is described by the Drude free electron theory [29, 30] as follows:

$$\varepsilon(\omega) = \varepsilon_\infty - \frac{\omega_p^2}{\omega^2 + i\Gamma_d \omega}, \quad (20)$$

$$\text{Re}(\varepsilon) = 1 - \frac{\omega_p^2}{\omega^2 + \Gamma_d^2}, \quad \text{Im}(\varepsilon) = \frac{\omega_p^2 \Gamma_d / \omega}{\omega^2 + \Gamma_d^2}, \quad (21)$$

where $1/\Gamma_d$ is the relaxation time or DC conductivity and ε_∞ is fixed to 1. The parameters of NiFe, namely $\omega_p = 14.79$ eV and $\Gamma_d = 4.78$ eV [31], are applied in this work.

Sellmeier equation [32] is used for the refractive index of quartz:

$$n^2 - 1 = \frac{B_1 \lambda^2}{\lambda^2 - C_1} + \frac{B_2 \lambda^2}{\lambda^2 - C_2} + \frac{B_3 \lambda^2}{\lambda^2 - C_3}, \quad (22)$$

where B_i and C_i ($i = 1, 2, 3$) are the dispersion constants listed below for λ in units of μm at 20°C [33]:

$$\begin{aligned} B_1 &= 0.473115591, & C_1 &= 0.0129957170, \\ B_2 &= 0.631038719, & C_2 &= 0.00412809220, \\ B_3 &= 0.906404498, & C_3 &= 98.7685322. \end{aligned} \quad (23)$$

2.3. Model of photoelectron emission

The other factors in Eq. (1) are considered in the case of thin semiconductors and visible light in the following. It was mentioned that $P_{\text{transport}}$ and P_{escape} can be lumped together and

$$P_{\text{transport}}(z, \lambda) P_{\text{escape}}(z, \lambda) = \begin{cases} G(\lambda) e^{-(d-z)/L_e} & \text{(front-illumination)} \\ G(\lambda) e^{-z/L_e} & \text{(back-illumination)} \end{cases} \quad (24)$$

is a good approximation [7], where $G(\lambda)$ is an undefined function of λ and L_e is the escape length of the excited electron in the photocathode. L_e depends on the inelastic and elastic scattering lengths. The electron-phonon scattering can be regarded as the elastic one because the energy loss by the scattering is quite small [34]. Scattering with electrons in the valence band can take place only if the electron in the conduction band has a sufficient energy to produce an electron pair over the band gap. The threshold energy was found to be more than twice the band gap above the bottom of the conduction band [35]. It was measured for (Cs)Na₃KSb photocathodes to be 3.0 eV [36], or 4.0 eV above the edge of the valence band, which corresponds to 310 nm wavelength of the photon absorbed. Scattering with impurities or defects could take place, but it is simply neglected here assuming that the photocathode thickness is sufficiently less than the scattering lengths for the impurities and

defects. Therefore L_e can be considered to be infinite in this work, and thus $P_{\text{transport}}P_{\text{escape}}$ is a function of λ only. This presumption shall be verified in Sec. 3.3.

When the electron reaches the vacuum surface, it can escape to the vacuum if it has a momentum of which the normal component with respect to the vacuum surface is greater than a critical value [8]. Namely the electron trajectory is required to fall within the escape cone of the apex angle $2\theta_c$ defined by $\cos \theta_c = \sqrt{\Phi/E_e} > \sqrt{\Phi/h\nu}$, where Φ is the work function, $E_e(> \Phi)$ is the energy of the electron at the vacuum surface and $h\nu(> E_e)$ is the energy of the absorbed photon. This requirement could be a significant reduction factor for the QE when the electron went straight from the initial position to the vacuum surface without any scatterings. The acceptance of the electron escape in this case would be $(1 - \cos \theta_c)/2 < 0.18$ for $\Phi = 1.55$ eV [7] and $\lambda = 320$ nm. It means that the QE at 320 nm or longer wavelengths would be limited to 18% at most. However the elastic electron-phonon scattering can enhance the escape probability because it gives the electron many chances to reach the vacuum surface at different angles as in the case of random walk [37]. Under the condition that the transportation is lossless, the electron can keep hitting the vacuum surface until it falls within the escape cone. Once it falls, the escape probability can be regarded as unity [11]. As far as only electrons above the vacuum level are counted, $P_{\text{transport}}P_{\text{escape}}$ therefore could be unity.

Consequently the three-step model is reduced to only one step: photoexcitation of an electron to an energy above the vacuum level with a probability $P_{\text{excite}}(\lambda)$ which is equal to the ratio of the probability of transitions above the vacuum level to the one of all transitions. P_{excite} depends on the work function and normally increases monotonically as a function of the photon energy. To exactly describe the P_{excite} function, one also has to consider the electron density of states which governs the transition probability as studied in Refs. [38–40]. However it is beyond the scope of this work, and P_{excite} is taken as a parameter to be determined independently at each wavelength.

2.4. QE function

In summary the QE is expressed by a function

$$QE(\lambda, \theta, \epsilon) = P_{\text{excite}}(\lambda)A_{\text{pc}}(\lambda, \theta, \epsilon), \quad (25)$$

$$A_{\text{pc}}(\lambda, \theta, \epsilon) = \int_0^{d_3} A'_3(z, \lambda, \theta, \epsilon)dz + T_{2+3}(\lambda, \theta, \epsilon)(1 - \mathcal{R}_{\text{OA}})R_{\text{el}}(\lambda, \theta, \epsilon) \int_0^{d_2} A'_2(z, \lambda, \theta, \epsilon)dz. \quad (26)$$

The parameters to be determined are P_{excite} for each λ , and respective d , ϵ_s , ω_t and Γ_0 of the photocathode and the antireflection coating. \mathcal{R}_{OA} is supposed to be 0.6. As a consequence of the one step model of photoelectron emission, the dependence of the QE on the angle θ and the polarization ϵ is dictated only by the optical properties.

3. Experimental verification

This section describes the measurement of the dependence of the QE on the angle and polarization. The QE function derived in the previous section shall be verified experimentally.

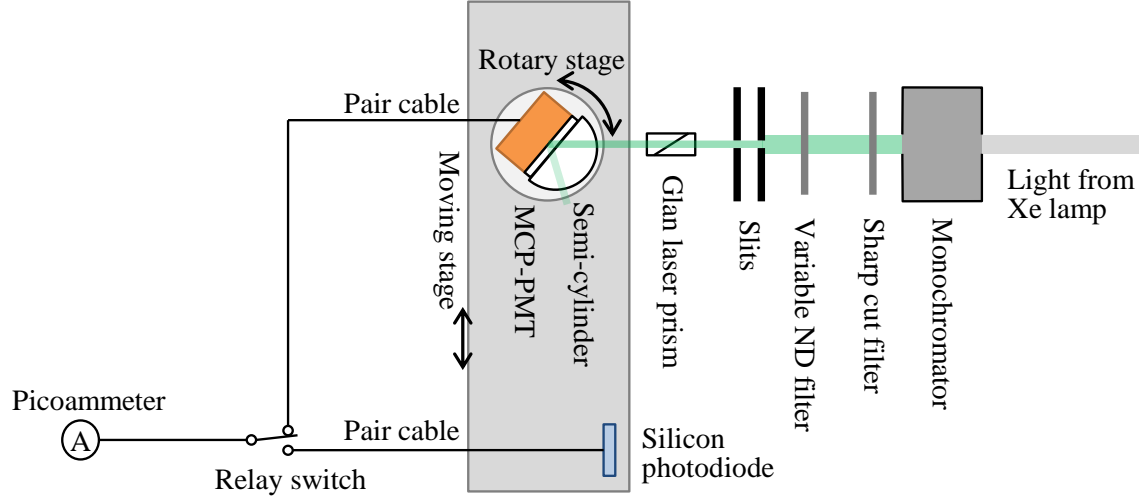


Fig. 3: Schematic top view of the setup of the QE measurement.

3.1. Measurement setup

The QE was measured as the photocurrent on the PMT photocathode under illumination of linearly polarized light. The data were taken at 81 incident angles (2° intervals from -80° to 80°) and at 18 wavelengths (20-nm intervals from 320 to 660 nm) for both polarizations in the setup shown in Fig. 3. The incident angle was selected by rotating the PMT on a rotary stage while fixing the optical system. The normal incident angle was defined as 0° . The light source was a xenon lamp, and the wavelength was selected by a monochromator. Two types of sharp cut filters were placed in a switchable holder and one of them or a blank was selected according to the wavelength in order to cut out stray light from the monochromator. Following a round continuously variable neutral density (ND) filter and two slits, a Glan laser prism was placed. It polarized the light with an extinction ratio less than 5×10^{-6} . The photocathode was illuminated through a semi-cylinder whose radius of the curvature was 15 mm and through the PMT window. The semi-cylinder and the window were both made of synthetic quartz and were coupled together via index-matching optical oil made of fused silica. Therefore the light passed from the air to the photocathode without refraction at any orientations of the PMT rotation as the PMT was rotated about the axis of the semi-cylinder. The light spotted around the center of the photocathode, of which the size was $23 \times 23 \text{ mm}^2$. The size of the light spot was about 1 mm in diameter. The photoinduced current on the photocathode I_{PMT} was read out by a picoammeter without any amplification. The light intensity was adjusted by the ND filter so that I_{PMT} did not exceed 10 nA to avoid saturation due to the space charge effect in the photocathode. The counter-current of the photoelectrons was got out to the MCP electrode by applying +200 V on it. A silicon photodiode was used to measure the light intensity. It was mounted on a moving stage together with the PMT rotary stage and took turns measuring the light. The photocurrent of the photodiode I_{PD} was measured by the same picoammeter as a relay switch selected either of the photodevices. Therefore $I_{\text{PMT}} \cdot QE_{\text{PD}}/I_{\text{PD}}$ amounts to the PMT QE, where the absolute QE spectrum of the photodiode $QE_{\text{PD}}(\lambda)$ was calibrated in advance with a precision of 0.5-1.7% depending on the wavelength. In this measurement the PMT QE was

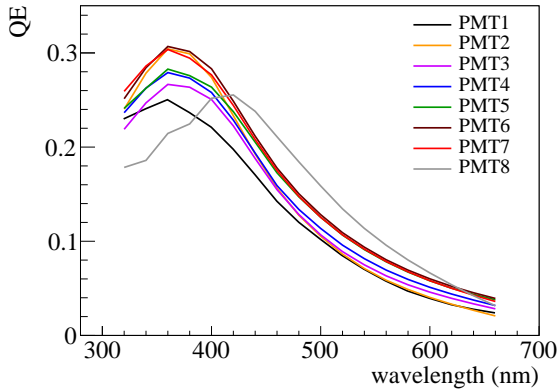


Fig. 4: Measured QE spectra at 0° . The error bars of the data are omitted in this figure.

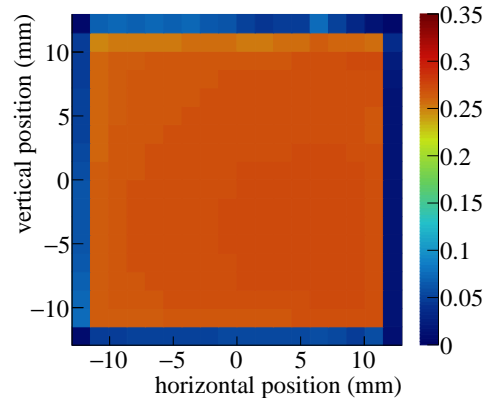


Fig. 5: QE distribution of PMT3 at 0° and 360° . The color represents the QE.

defined as the efficiency of detecting the incident light onto the quartz semi-cylinder, and about 4% loss by the reflection at the air-quartz interface was counted as the inefficiency.

The measurement for both rotation directions (from 0° to $\pm 80^\circ$) was intended for canceling out the error due to misalignments of the PMT position and angle. In the analysis the QEs at the same absolute angle were averaged and the difference of the QEs was considered as the error.

Compared to the standard technique of reflectance measurement, this photocurrent measurement has some advantages; Another photodevice to measure the reflected light is unnecessary, and therefore the difficulties can be avoided in aligning that photodevice in accordance with the angle of the incident light, in particular around 0° where the incident and reflected light overlaps; In addition the measurement uncertainties related to that photodevice can be omitted; Regarding the dependence of the QE on the angle and polarization, it should be measured directly by the photocurrent as it is in general not trivial to interpret the absorbance deduced by the reflectance measurement as the QE.

3.2. Results

Eight PMTs (called hereafter PMT1-8) of the same type of photocathode were measured. Though all the photocathodes were produced in the same way, some differences of the QE spectra measured at 0° are recognizable in Fig. 4. While PMT1-7 have similar spectra, PMT8 differs from the others: the former spectra peak around 360 nm and the latter peaks around 420 nm. The QE at the peak varies PMT-by-PMT from 24.9 to 30.6%. Within the individual PMTs the QE is uniform over the photocathode. It was confirmed in advance by measuring the QE at 18×18 points over the photocathode including the fringe at 0° without the semi-cylinder. A typical example is shown in Fig. 5 for PMT3.

The QEs measured as a function of the incident angle are shown in Fig. 6. The broad feature of the curve is similar for all the PMTs except PMT8. The prominent rise (valley) of the QE for s(p)-polarization around 43° mentioned in Sec. 2.1 cannot be seen for PMT8.

The function of Eq. (25) was fitted to the QE data of each PMT. The fitting was done simultaneously for both polarizations, all the 18 wavelengths (320-660 nm) and all the 41

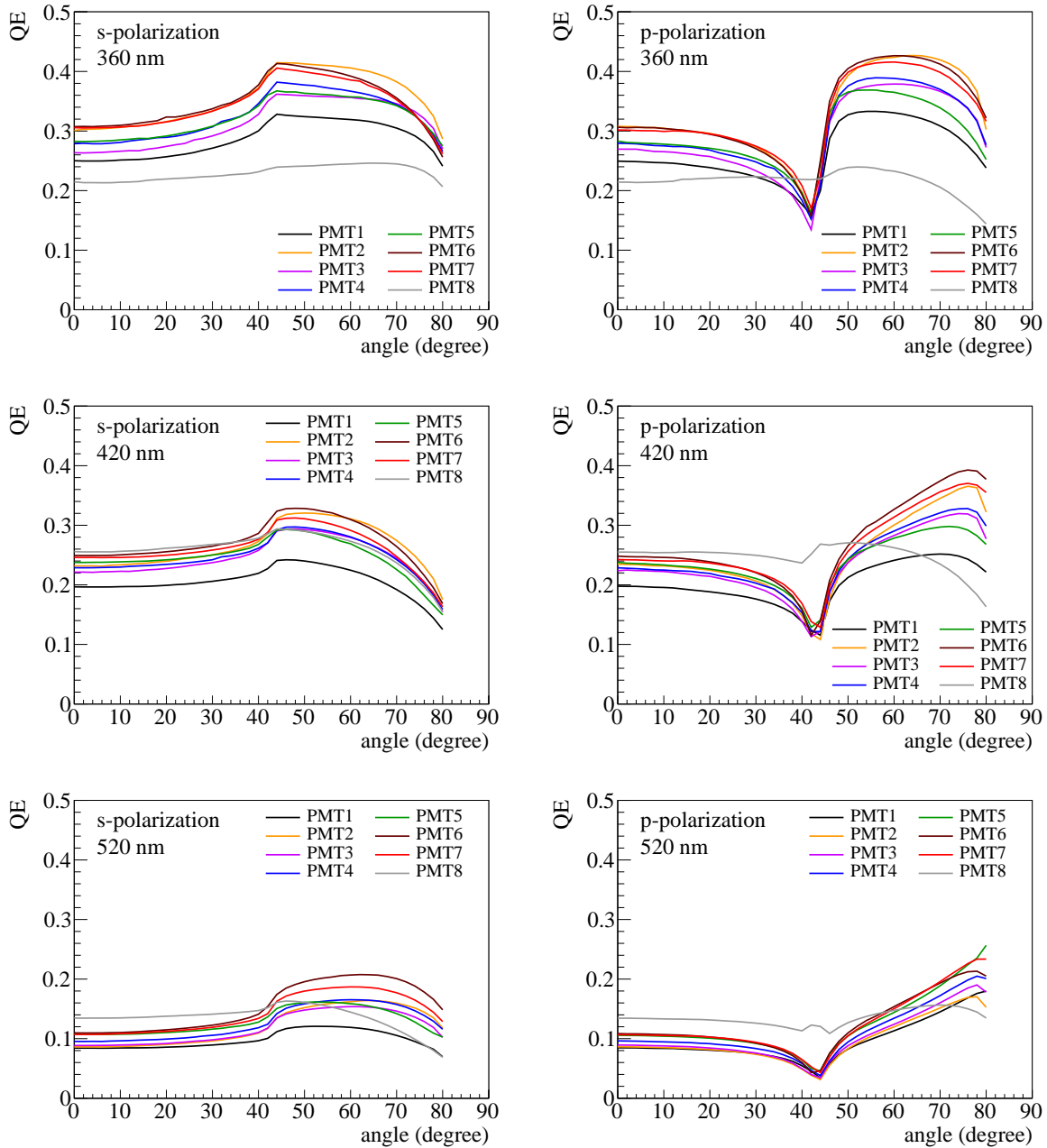


Fig. 6: Measured QE as a function of the incident angle for s-polarized (left) and p-polarized (right) light. The data only at 360 nm (top), 420 nm (middle) and 520 nm (bottom) wavelengths are shown in this figure. The error bars of the data are omitted.

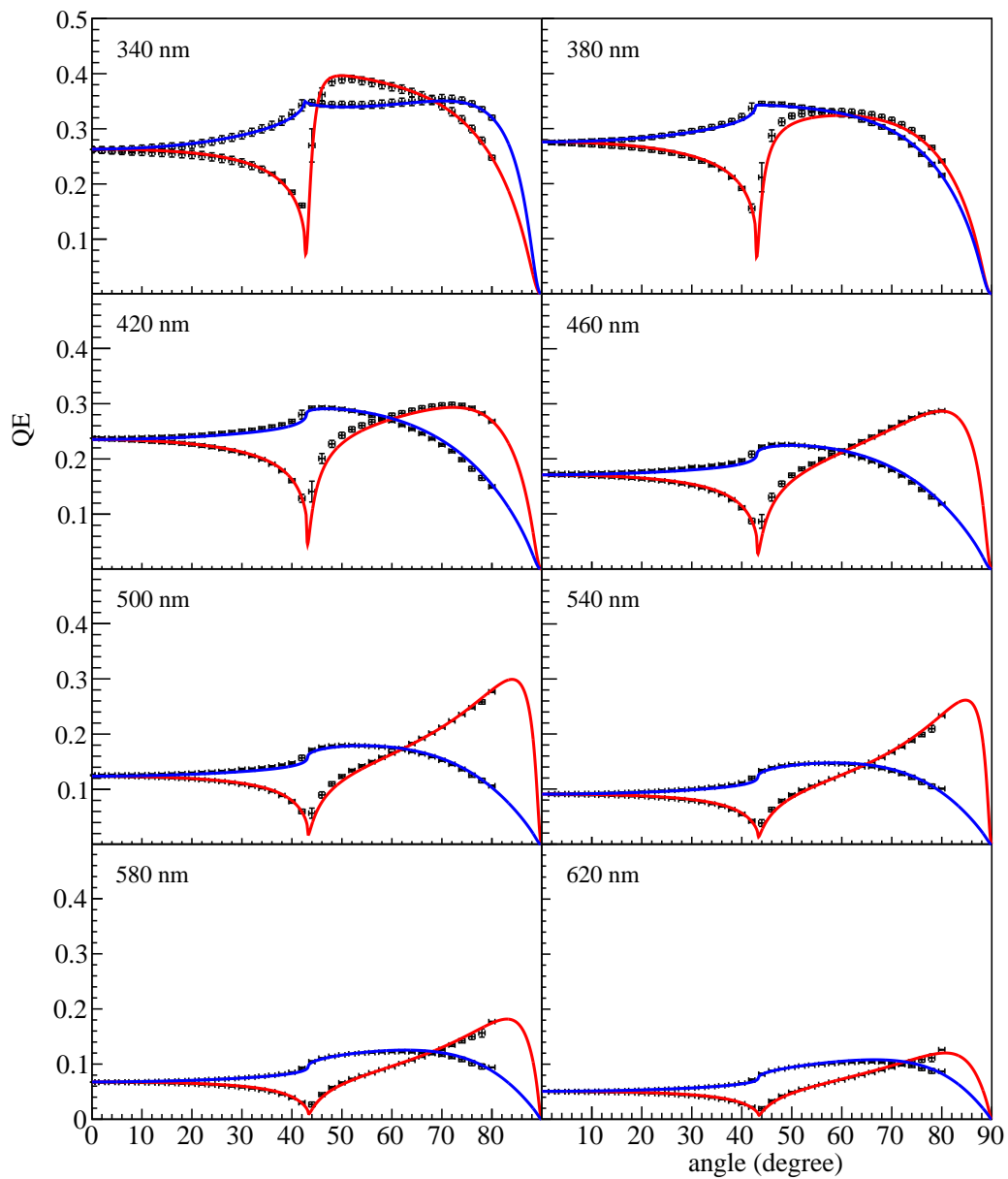


Fig. 7: Fitted function (blue lines for s-polarization and red ones for p-polarization) overlaid on the data (dots with error bars) for PMT5. Only those at 340, 380, 420, 460, 500, 540, 580 and 620 nm wavelengths are shown in this figure.

angles (0-80°) using chi-squared minimization. Comparisons between the data and the fitted function can be seen for PMT5 as an example in Fig. 7. The error bars on the data points in this figure include statistical and all systematical errors. It is remarkable that the single function fits all the data of the PMT almost perfectly. For the other PMTs the agreement between the data and the fitted function is similar or better. It indicates that the Lorentz dispersion model and the one step model of the photoelectron emission are appropriate for this type of photocathodes. The best fit parameters are shown in Table 1 and Fig. 8. No significant differences of the thickness and the optical parameters are identified for the antireflection coating. On the other hand, the photocathode has a variation of the thickness. Especially the one of PMT8 is thicker than the others. It distinguishes the photocathode response as being different from the others as seen in Figs. 4 and 6; A thicker photocathode is more sensitive at longer wavelengths, and has less QE variation along with the angle. Another variation of the photocathode can be seen in ϵ_s , while the other optical parameters are consistent with each other. P_{excite} seems to be a monotonically increasing function of the photon energy though the uncertainty is rather large. P_{excite} of PMT8 shows a slightly different feature as it declines a little below 400 nm. It might be a sign of the scattering loss to be discussed in the next section or a fake due to the large uncertainty of P_{excite} .

3.3. QE reduction by the scattering

If the scattering loss was not negligible, its effect should appear in the shape of the QE-angle curve in Fig. 6. The QE expression in Eq. (25) then needs to be modified by getting $P_{\text{transport}}P_{\text{escape}}$ of Eq. (24) back into the integral:

$$\begin{aligned}
QE(\lambda, \theta, \epsilon) &= \mathcal{P}_{\text{excite}}(\lambda)e^\beta \left[a|v|^2 \int_0^d e^{(-2\text{Im}(\tilde{\nu})+\alpha)z} dz + a|w|^2 \int_0^d e^{(2\text{Im}(\tilde{\nu})+\alpha)z} dz \right. \\
&\quad \left. + 2b\text{Re}(vw^*) \int_0^d \cos(2\text{Re}(\tilde{\nu})z)e^{\alpha z} dz - 2b\text{Im}(vw^*) \int_0^d \sin(2\text{Re}(\tilde{\nu})z)e^{\alpha z} dz \right] \\
&= \mathcal{P}_{\text{excite}}(\lambda)e^\beta \left[a|v|^2 \frac{e^{(-2\text{Im}(\tilde{\nu})+\alpha)d} - 1}{-2\text{Im}(\tilde{\nu}) + \alpha} + a|w|^2 \frac{e^{(2\text{Im}(\tilde{\nu})+\alpha)d} - 1}{2\text{Im}(\tilde{\nu}) + \alpha} \right. \\
&\quad \left. + 2b\text{Re}(vw^*) \frac{e^{\alpha d} \{ \alpha \cos(2\text{Re}(\tilde{\nu})d) + 2\text{Re}(\tilde{\nu}) \sin(2\text{Re}(\tilde{\nu})d) \} - \alpha}{4(\text{Re}(\tilde{\nu}))^2 + \alpha^2} \right. \\
&\quad \left. - 2b\text{Im}(vw^*) \frac{e^{\alpha d} \{ \alpha \sin(2\text{Re}(\tilde{\nu})d) - 2\text{Re}(\tilde{\nu}) \cos(2\text{Re}(\tilde{\nu})d) \} + 2\text{Re}(\tilde{\nu})}{4(\text{Re}(\tilde{\nu}))^2 + \alpha^2} \right], \\
\alpha &= \frac{1}{L_e}, \quad \beta = -\frac{d}{L_e} \quad (\text{front-illumination}) \\
\alpha &= -\frac{1}{L_e}, \quad \beta = 0 \quad (\text{back-illumination})
\end{aligned} \tag{27}$$

Here the second term of Eq. (26) for the back-illumination is not explicitly written and the subscript l is omitted. P_{excite} is redefined as $\mathcal{P}_{\text{excite}}$ to lump G together. Equation (27) with $L_e = \infty$ is identical to Eq. (25). With a finite L_e the QE is reduced as shown in Fig. 9 (left), where Eq. (27) with $\theta = 0^\circ$ is plotted as a function of L_e while the other parameters are fixed to the values in Table 1 and Fig. 8.

In order to compare the angular dependences of the QE with different L_e 's, the optical parameters are fixed but $\mathcal{P}_{\text{excite}}$ is adjusted to normalize the QE to the one of the data at

Table 1: Thickness and the optical parameters of the photocathode and the antireflection coating obtained by the fitting. The reduced χ^2 of the fit is also shown in the last column. The last row shows the average of the eight PMTs.

PMT	Photocathode				Antireflection coating				χ^2/ndf
	d (nm)	ε_s	ω_t (eV)	Γ_0 (eV)	d (nm)	ε_s	ω_t (eV)	Γ_0 (eV)	
1	11.5±3.9	8.3±2.5	3.13±0.09	1.24±0.21	32.7±5.4	4.6±0.6	16.9± 2.5	3.6±3.0	2.41
2	9.4±3.9	7.4±2.3	3.28±0.09	1.28±0.26	36.2±6.0	3.8±0.7	9.8± 8.3	1.2±2.9	1.31
3	7.8±4.0	8.1±3.2	3.20±0.09	1.11±0.20	36.1±5.4	4.4±0.4	15.7±11.0	4.7±2.8	2.84
4	10.0±4.1	7.5±2.4	3.19±0.09	1.14±0.14	33.7±5.6	4.2±0.4	13.3± 3.7	2.4±1.4	1.50
5	10.4±4.0	8.0±2.6	3.24±0.08	0.97±0.15	37.7±4.3	4.4±0.4	16.4± 6.5	3.4±3.8	3.20
6	6.2±5.1	9.4±8.2	3.24±0.09	0.96±0.18	30.3±7.4	4.5±0.8	13.0± 9.6	3.9±2.6	1.61
7	9.2±5.6	7.6±3.4	3.23±0.09	1.05±0.22	30.7±6.1	4.6±0.7	17.0±10.6	4.0±4.3	1.43
8	37.0±5.9	5.9±1.0	3.31±0.33	1.35±0.66	40.4±5.2	4.7±0.8	16.0±11.5	4.9±3.6	3.85
Avg.	NA	6.8±0.7	3.22±0.03	1.09±0.07	35.4±1.9	4.4±0.2	15.5± 1.8	3.1±0.9	–

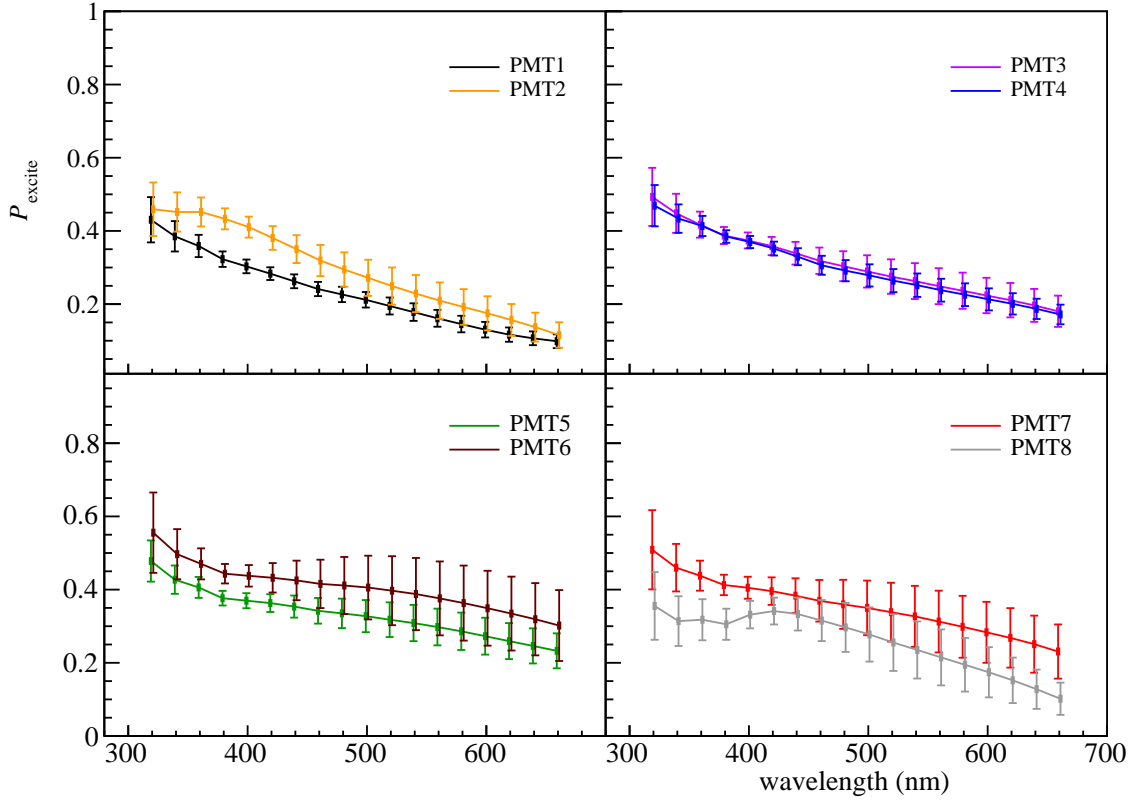


Fig. 8: P_{excite} obtained by the fitting.

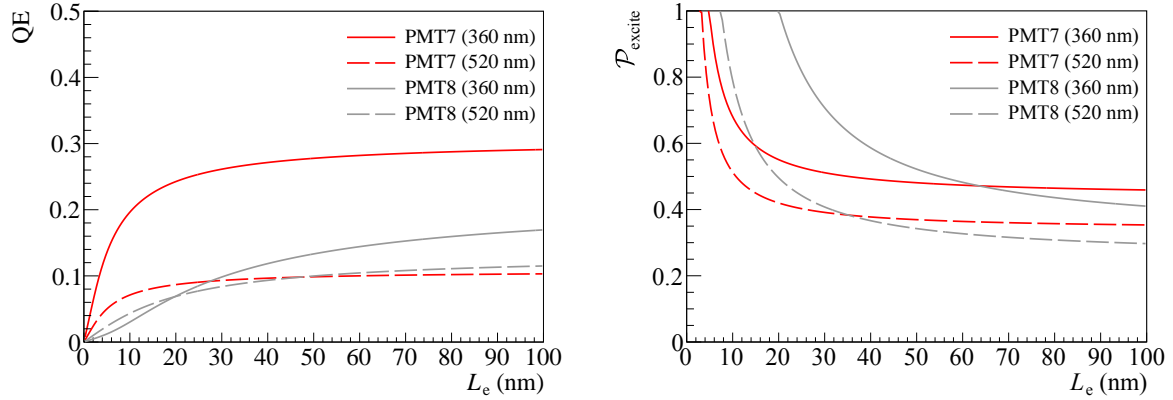


Fig. 9: (Left) Variation of the QE at 0° as a function of the escape length when $\mathcal{P}_{\text{excite}}$ is fixed to the one for $L_e = \infty$ or $\mathcal{P}_{\text{excite}}$. (Right) $\mathcal{P}_{\text{excite}}$ which makes the QE function normalized to the data at 0° depending on the escape length. Those for PMT7 and 8 at 360 and 520 nm wavelengths are shown in these plots.

0° . $\mathcal{P}_{\text{excite}}$ to be applied as a function of L_e is shown for PMT7 and 8 in Fig. 9 (right). It indicates a distinct lower limit on L_e that is longer than about a half of the photocathode thickness as $\mathcal{P}_{\text{excite}} < 1$ by definition, if Eq. (24) holds. After the normalization the effect of L_e on the angular dependence of the QE can be seen in Fig. 10. The effect for s-polarization is found to be little. The one for p-polarization is rather visible when L_e is comparable with the photocathode thickness as the angular dependence starts to differ from the data. The difference is larger when L_e is about a half of the thickness, which is though not feasible as mentioned above. Therefore one can estimate that L_e is larger than the photocathode thickness. It is consistent with the measured L_e reported in Ref. [41]. If L_e is close to the photocathode thickness, the reduction of the QE is significant. With $L_e = 10$ nm, for example, the QE at 0° and 360 nm wavelength is reduced to 64% of the one with $L_e = \infty$ for PMT7. Therefore the PMT-by-PMT difference of $\mathcal{P}_{\text{excite}}$ could be due to a difference of L_e .

Although the actual value of L_e is unclear, we can conclude that $P_{\text{transport}}P_{\text{escape}} \approx G(\lambda)$ is a good approximation to describe the angular dependence of the QE. Actually it is hard to fit the QE function with a short L_e to the data because the optical parameters are strongly constrained by the angular dependence of the QE for s-polarization independently of L_e and only L_e can be then floated to fit the function in the one for p-polarization. Consequently, to interpret the QE function more properly, Eq. (25) should be rewritten as

$$QE(\lambda, \theta, \epsilon) = \mathcal{P}_{\text{excite}}(\lambda)A_{\text{pc}}(\lambda, \theta, \epsilon). \quad (28)$$

$\mathcal{P}_{\text{excite}}$ is regarded as the probability of photoexcitation of an electron to an energy above the vacuum level plus a certain amount of energy loss by the scatterings.

4. Optical properties of the photocathode

As denoted in Eq. (25) the optical properties of the photocathode as well as those of the antireflection coating are of great importance in the QE and its angular dependence. In the following they are discussed using the optical parameters obtained in the previous section.

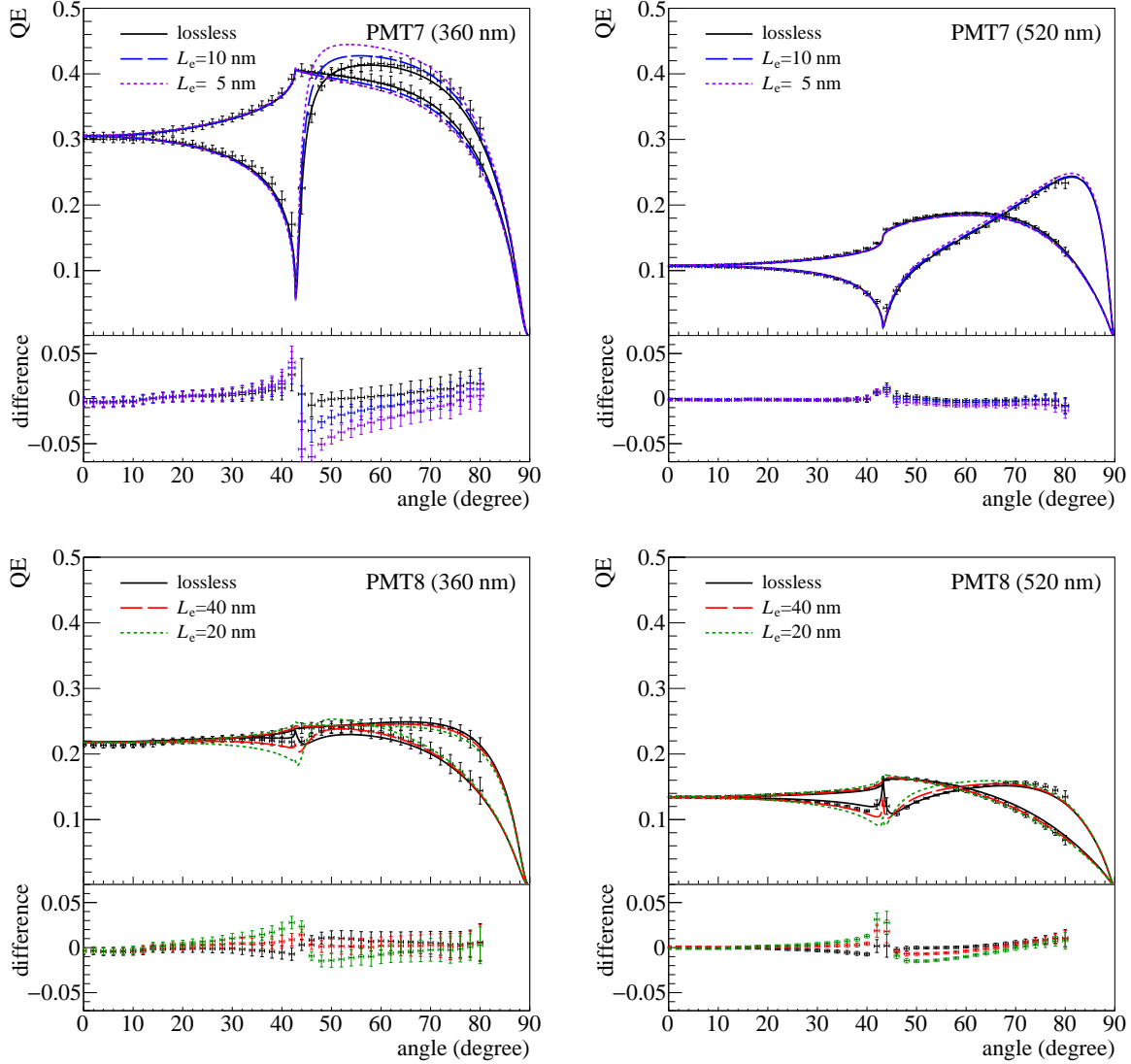


Fig. 10: Expected angular dependence of the QE at 360 nm (left) and 520 nm (right) with different escape lengths L_e for PMT7 (upper) and PMT8 (lower). The QE curves both for s- and p-polarizations are plotted in the same upper panels. The dots with error bars represent the data. The differences of the data from each curve are shown only for p-polarization in the lower panels.

4.1. Refractive index and absorptance of the photocathode

Figure 11 shows the refractive index ($n + ik$) of PMT5 photocathode derived from Eqs. (18) and (19) using the best fit parameters in Table 1. The peak of n and k is around 420 nm and 360 nm, respectively. The spectrum of k is similar to the one of the QE shown in Fig. 4 as k relates to the absorption. For comparison Fig. 11 also includes previously published data for multi-alkali photocathodes composed of the same elements (NaKSbCs) and windows of two different materials: Jones [24] and Chyba [25] for borosilicate windows; Ghosh [20], Hallensleben [21] and Harmer [23] for fused silica windows. The index measured in this work differs at the shorter wavelengths from Ghosh, Hallensleben and Harmer. Especially

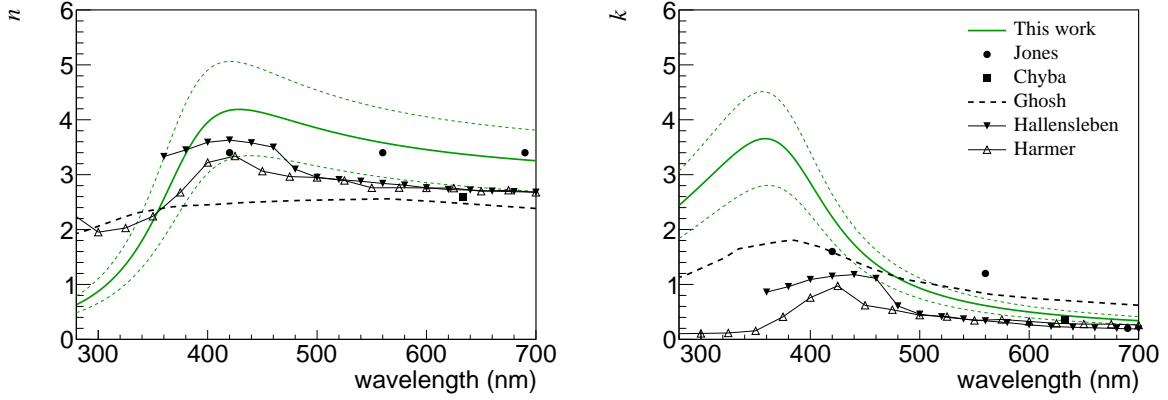


Fig. 11: Real (left) and imaginary (right) parts of the refractive index of the photocathode for PMT5. The solid and dotted green lines represent the best fit dispersions and the 1σ allowed bands, respectively. The previously published data for the same type of photocathodes are also plotted for comparison.

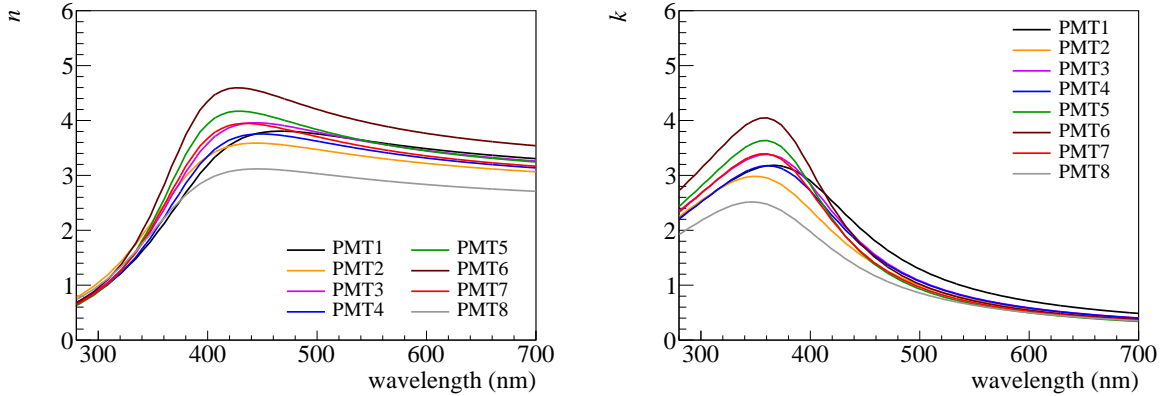


Fig. 12: Real (left) and imaginary (right) parts of the refractive index of the photocathode. Only the best fit dispersions are plotted in this figure.

the discrepancy in k with Harmer is quite large, but $k \sim 0$ below 350 nm or insensitivity to near-ultraviolet light is rather strange for the multi-alkali photocathode.

The dispersion curves for the other PMTs are plotted in Fig. 12. They are more or less consistent within the errors. The difference at the best fit is attributed to the different ϵ_s of the photocathode. The respective peak wavelengths of n and k are almost the same for all the PMTs since ω_t 's are consistent within the errors.

The total absorptions of the photocathodes at 0° calculated using Eq. (16) are shown in Fig. 13 (left). They are nearly the same at wavelengths below 400 nm. The difference above 400 nm comes mainly from the difference of the photocathode thickness. Given the same thickness of 10.0 nm for all the photocathodes, the absorption spectrum is similar to each other as shown in Fig. 13 (right). The remaining difference seen in this figure between PMT8 and the other PMTs originates from ϵ_s of the photocathode, but it is within the error

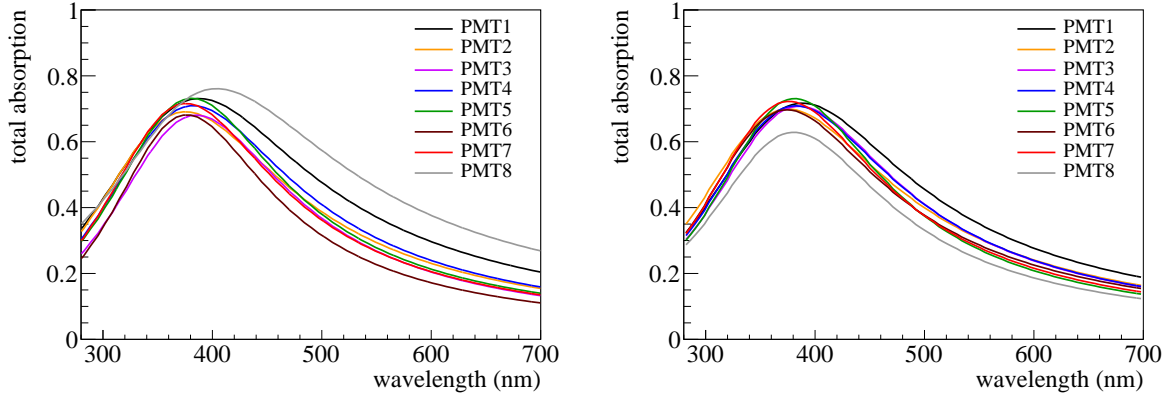


Fig. 13: Total absorption of the photocathode at 0° including the back-illumination. (Left) Calculated with the best fit parameters in Table 1. (Right) Calculated with the same parameters other than the photocathode thickness, which is fixed to 10.0 nm for all the photocathodes.

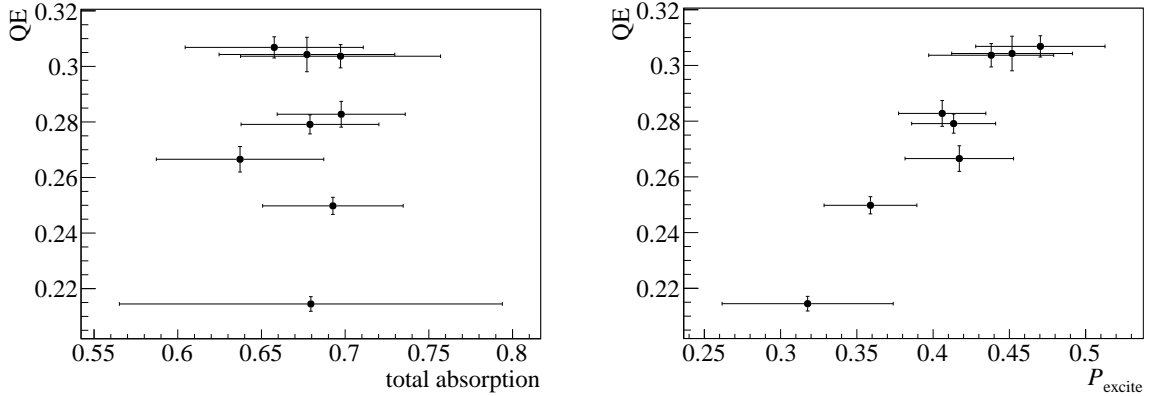


Fig. 14: Correlation of the QE at 0° with the total absorption (left) and with P_{excite} (right) at 360 nm.

range. Compared to the QE spectrum in Fig. 4, therefore, the variation of the QE can be attributed not to the optical property of the photocathode other than the thickness but to P_{excite} . It can be clearly seen in Fig. 14, where the QE at 0° is plotted relative to the total absorption or P_{excite} at 360 nm for the eight PMTs. The QE has a correlation not with the total absorption but with P_{excite} (or $\mathcal{P}_{\text{excite}}$), which is subject to the work function and the escape length.

4.2. Effect of the back-illumination

The QE was measured as a sum of the front- and back-illuminations. As denoted in Eq. (16) the back-illumination is reduced by the factors T_{2+3} , $1 - \mathcal{R}_{\text{OA}}$ and R_{el} , and it should have less contribution to the QE. Figure 15 shows T_{2+3} , $T_{2+3}(1 - \mathcal{R}_{\text{OA}})R_{\text{el}}$ and $T_{2+3}(1 - \mathcal{R}_{\text{OA}})R_{\text{el}}A_2$ at 360 nm as a function of the incident angle θ_1 . T_{2+3} is 0.257 at 0° and increases as the angle

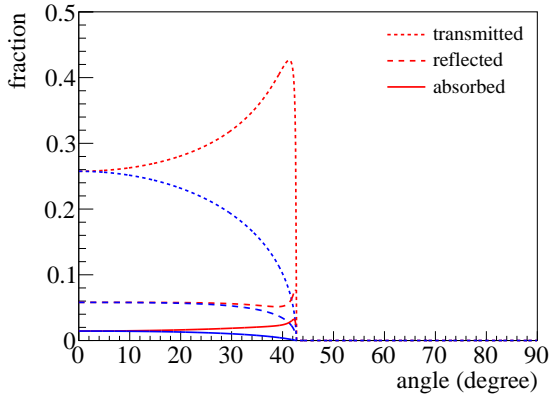


Fig. 15: Intensity fraction of 360 nm light transmitted through PMT7 photocathode (dotted line), one of the back-illumination after reflection on the electrode (dashed line) and one of the back-illumination absorbed by the photocathode (solid line) with respect to the initial light. The blue (red) lines represent those for s(p)-polarization.

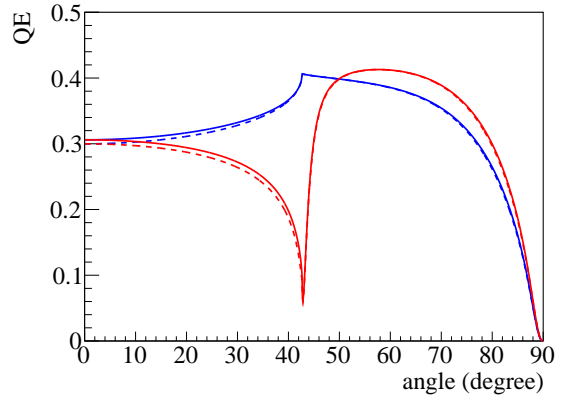


Fig. 16: QE at 360 nm as a function of the incident angle calculated with and without the back-illumination (solid and dashed lines, respectively) for PMT7. The blue (red) lines represent those for s(p)-polarization.

for p-polarization, while it decreases for s-polarization. Hence the contribution of the back-illumination is larger for p-polarization. The following discussion takes the case of the normal incidence at 360 nm. The factor $(1 - \mathcal{R}_{\text{OA}})R_{\text{el}}$ reduces the fraction of the back-illumination down to 0.058. In addition the reflection at the vacuum-photocathode interface for the back-illumination is higher than the one at the quartz-photocathode interface for the front-illumination due to a larger mismatch of the refractive indices. For example, the reflectance of the photocathode $|\hat{r}|^2$ for the back- and front-illumination is 39.8% and 21.8%, respectively, where the antireflection coating is omitted for simplicity and the parameters of PMT7 photocathode are used. It further reduces the fraction of the absorbed back-illumination down to 0.014, resulting in 0.6% QE regarding only the back-illumination. The effect of the back-illumination is feeble at any angle as shown in Fig. 16.

Even if a more reflective material is put behind the photocathode to fully reflect the transmitted light, the enhancement of the QE cannot be significant. The maximum possible contribution of the back-illumination at 0° , namely under assumption of $(1 - \mathcal{R}_{\text{OA}})R_{\text{el}} = 1$, is shown in Fig. 17. The factor of enhancement by the full back-illumination is only 1.09 at 360 nm for this photocathode with the antireflection coating. It is inversely-related to the QE for the front-illumination since the transmittance of the photocathode decreases as the absorptance increases. Therefore the fraction of the back-illumination becomes larger away from the wavelength of the peak QE, but the net QE increase by the full back-illumination is nearly constant about 1-3% regardless of the wavelength. In the same manner the ratio of the back-illumination becomes larger without the antireflection coating. The increase of the QE by the antireflection coating is, however, larger than the one by the back-illumination at the

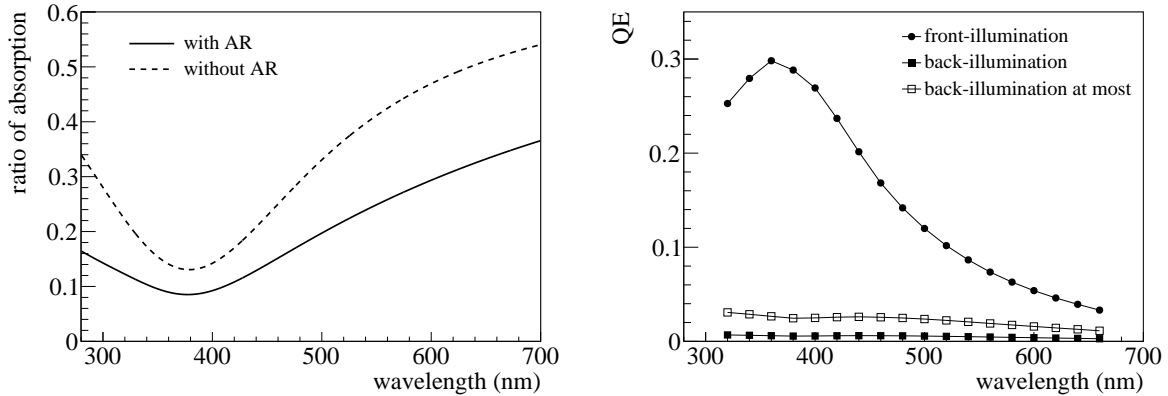


Fig. 17: (Left) Ratio of the absorbed back- to front-illumination at 0° when $(1 - \mathcal{R}_{OA})R_{el}$ is assumed to be unity. It is calculated for PMT7 photocathode with and without the antireflection coating (AR). (Right) Respective contributions of the front- and back-illuminations to the QE at 0° for PMT7 photocathode with the antireflection coating. Both the actual and the maximum possible back-illumination are plotted.

peak wavelength, and removing the antireflection coating to increase the back-illumination adversely decreases the QE.

Another attempt is to put the second photocathode of reflection mode which detects transmitted light through the first photocathode [42]. For the same reason mentioned above, however, one can expect a little improvement of the QE, while the dark noise rate increases in proportion to the photocathode area.

Since the contribution of the back-illumination is little for the PMTs in this work, only the front-illumination is considered in the following discussions.

4.3. Effect of the antireflection coating

Figure 18 shows the refractive index ($n + ik$) of the antireflection coating derived from Eqs. (18) and (19) using the best fit parameters in Table 1. The dispersion in this range of wavelength is quite small; n is about 2.15 and k is nearly 0. The thickness of the antireflection coating ranges from 30.3 to 40.4 nm. These values of the index and the thickness are adequate for destructive interference of the reflected light waves to reduce the reflection. The effect of the antireflection coating on the QE is manifest as shown in Fig. 19. The factor of enhancement of the QE is 1.18 at 360 nm and 0° . More significant enhancement can be seen at large incident angles for s-polarization. On the other hand the QE at 460 nm or longer is reduced by the antireflection coating due to the interference other way around. Although the antireflection coating has a nonzero value of k and absorbs the light, it is not the main cause of the reduction. The absorptance of the antireflection coating is, for example in the case of PMT7, 6.2% at 360 nm and almost constant at 1.2% above 500 nm.

Adjustment of the thickness of the antireflection coating could help to enhance the QE at a desired range of the wavelength. Given the refractive indices of the window, antireflection coating and photocathode, the best matching thickness of the antireflection coating can be estimated. Figure 20 shows the dependence of the absorptance of the photocathode on the

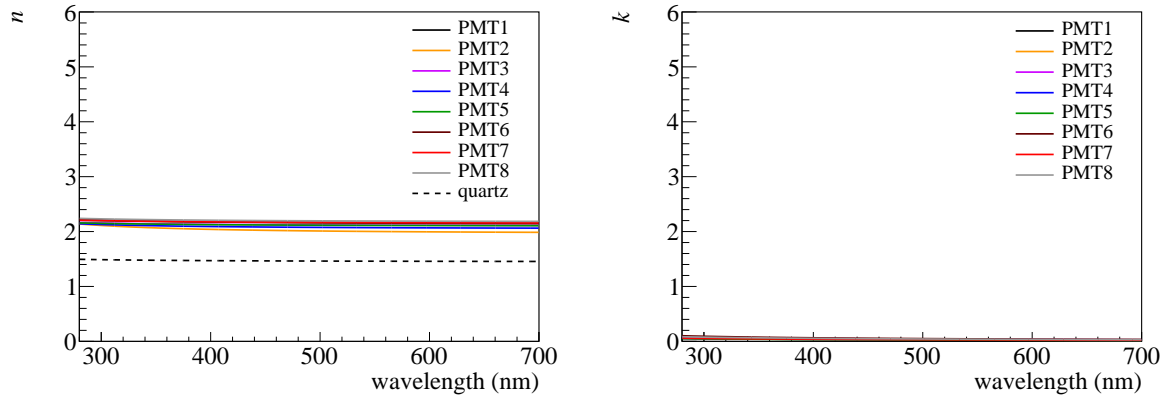


Fig. 18: Real (left) and imaginary (right) parts of the refractive index of the antireflection coating. The one of quartz is also shown for comparison.

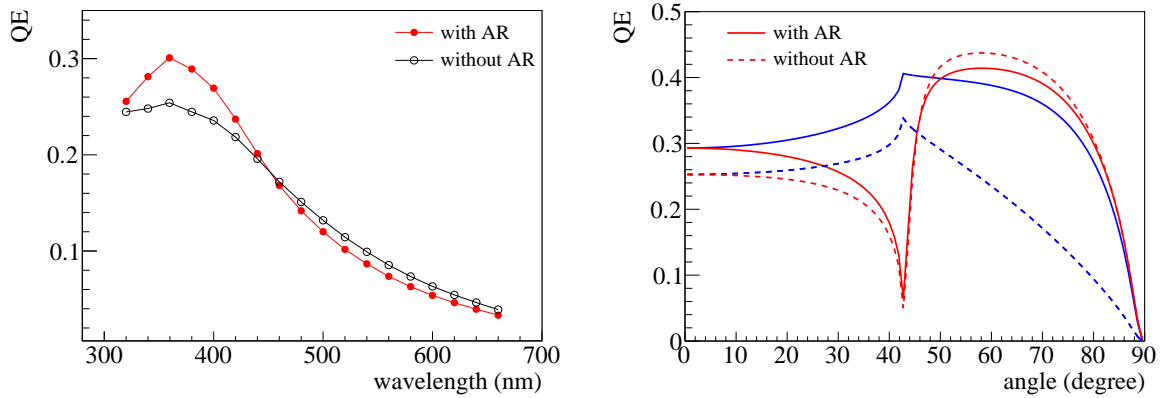


Fig. 19: Comparisons of the QE for PMT7 calculated with and without the antireflection coating (AR). Only the front-illumination is taken into account. (Left) QE at 0° as a function of the wavelength. (Right) QE at 360 nm as a function of the incident angle. The blue (red) lines represent the QE for s(p)-polarization.

thickness of the antireflection coating, where the other parameters than the thickness are the same as PMT7. The absorptance is maximized at the thickness of 28.7 nm, 50.4 nm and 86.3 nm for the wavelength of 360 nm, 420 nm and 520 nm, respectively. By adjusting the thickness to these values, the absorptance increases by 0.1%, 7.6% and 20.2%, respectively, from the one at the actual thickness of 30.7 nm.

4.4. Photon absorption in depth

Another parameter which could be tuned to enhance the QE is the thickness of the photocathode. In terms of the absorptance a thicker photocathode is better especially for longer wavelengths. It is also better in terms of the QE under the condition of the one step model, where the QE is simply proportional to the absorptance. Nevertheless for a thick photocathode comparable to the electron escape length, one has to take into account the scattering

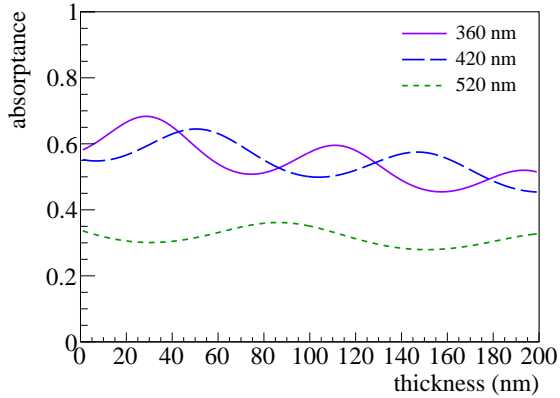


Fig. 20: Absorbance of PMT7 photocathode at 0° as a function of the thickness of the antireflection coating. There are three curves for 360, 420 and 520 nm wavelengths. Only the front-illumination is taken into account.

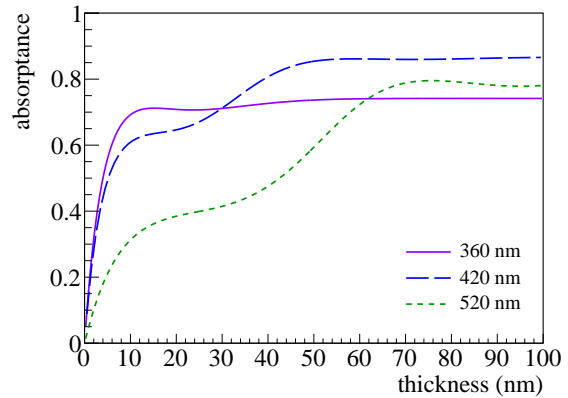


Fig. 21: Absorbance of PMT7 photocathode at 0° as a function of the photocathode thickness. There are three curves for 360, 420 and 520 nm wavelengths. Only the front-illumination is taken into account.

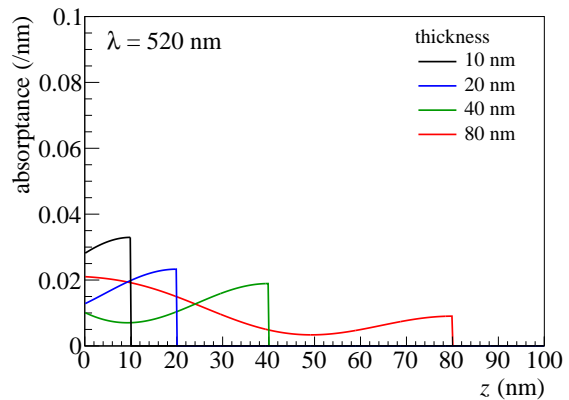
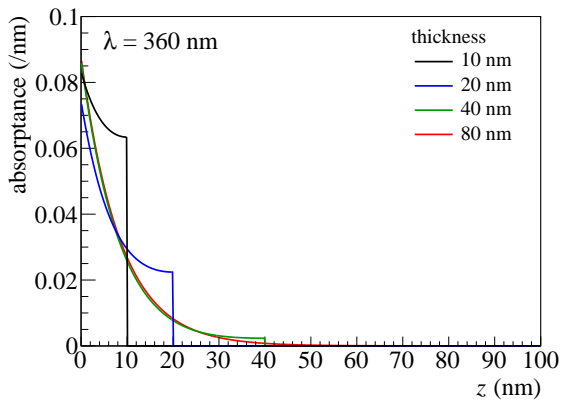


Fig. 22: Absorbance per unit length at 360 nm (left) and 520 nm (right) wavelengths as a function of the depth from the photocathode surface. There are four curves for different photocathode thicknesses, 10, 20, 40 and 80 nm. The refractive indices of the photocathode and antireflection coating for PMT7 are used in these plots. Only the front-illumination is taken into account.

loss. The optimal thickness can be foreseen in Fig. 21, where the absorbance is plotted as a function of the photocathode thickness by using Eq. (14). In terms of the QE at 360 nm, the absorbance at 10 nm thickness is close to its maximum, and a thicker photocathode could result in a less QE as only the scattering loss increases. Therefore the thickness around 10 nm is optimal for the QE at 360 nm. To enhance the QE at longer wavelengths, for example up to 520 nm, the optimal thickness should be around 70 nm or less.

The absorbance per unit length expressed by Eq. (10) is shown in Fig. 22. It is different from the often-used Lambert-Beer law, $e^{-\alpha z}$, described by an absorption coefficient α . That

is due to the light waves reflected at the interfaces and their interference. Only when the photocathode is enough thick, the absorptance can be approximated by $e^{-\alpha z}$ as the light wave heading forward is fully absorbed before reflected. An example can be found in Fig. 22 for 80 nm thickness and 360 nm wavelength. The assumption of an infinite thickness, which is usually taken, is therefore not appropriate for a thin photocathode.

4.5. Prospect for enhancement of the QE

A straightforward way to enhance the QE is to put the photocathode aslant so that the light strikes at 50-80°, where the QE is higher than the one at 0° as shown in Fig. 6. Because it is discussed elsewhere [43, 44], other possibilities are mentioned here in terms of enhancement of the intrinsic QE for the same type of photocathodes. As discussed above there is a little room for improvement of the peak QE by adjusting the thicknesses of the antireflection coating and the photocathode. The strong correlation of the QE with P_{excite} found in Fig. 14 indicates that one of the dominant factors dictating the QE could be the work function. Because the low work function of the NaKSbCs photocathode is derived from a Cs-Sb dipole monolayer [45], matters to the QE could be, for example, the arrangement of surface atoms [46], the monolayer coverage [47], or the surface roughness [48]. Less significant in the QE should be the bulk of the photocathode, which dictates the optical properties, though impurities and defects in the bulk could be another dominant factor of the QE reduction.

5. Conclusion

Precise description of the PMT response requires formulation of the dependence of the QE on the angle and polarization of the incident photon, which was yet to be studied. Hence I proposed the one step model of photoelectron emission, or photoexcitation of an electron to an energy above a certain threshold for the emission, which is adequate for thin multi-alkali photocathodes and for visible light. In this model the dependence of the QE on the angle and polarization is fully involved in the absorptance, and thus it can be rigorously described by the optics theory. The theoretical function of the QE derived in this work precisely fit the measured dependence of the photocurrent on the angle and polarization at all the wavelengths from 320 to 680 nm simultaneously. That demonstrated the picture of the photoelectron emission rendered by the one step model.

The measurement furnished the new data of the refractive index of the NaKSbCs photocathode over the whole visible range. It revealed the optical properties of the photocathode and the following new insights were obtained. It was firstly demonstrated that the dispersion of the refractive index of NaKSbCs can be described by the Lorentz model. The gain in QE by reabsorbing the transmitted light through the photocathode is feeble because of the low transmittance of the efficient photocathode and the large reflection at the vacuum-photocathode interface. The QE differences among the photocathodes of the same type are attributed dominantly to the thickness of the photocathode and P_{excite} . It implies that a key of the QE enhancement could be the condition of the photocathode surface on the vacuum or the degree of crystalline perfection of the bulk.

In terms of the methodology for deducing the refractive index and thickness of the photocathode, the measurement of the photocurrent has proven to be useful in this work. It was also demonstrated for the first time that this method can be applied for the stratified

antireflection coating and photocathode and that the refractive indices and thicknesses of both layers can be deduced at the same time.

To conclude, the expression of the QE derived in this work enables the accurate measurement of the optical properties for thin multi-alkali photocathodes in the visible range and hence the precise description of the PMT response. It should be valid for the other types of thin photocathodes as long as the applicable range of the wavelength is reevaluated based on the threshold energy for the electron-electron scattering during the transportation, and if the Lorentz dispersion model is appropriate for those photocathodes.

Acknowledgment

This work was supported by JSPS KAKENHI Grant-in-Aid for Challenging Exploratory Research (Grant Number JP26610068). The MCP-PMTs measured in this work were produced for the Belle II TOP counter with support from JSPS KAKENHI Grant-in-Aid for Scientific Research (S) (Grant Number JP26220706). I would like to thank my colleagues at Nagoya University for discussion, in particular T. Iijima and K. Inami. I have also benefited from discussion with H. Watanabe, Y. Hasegawa, H. Nishizawa and H. Yamaguchi (HAMAMATSU PHOTONICS K.K.).

References

- [1] P. A. Cherenkov, C.R. Acad. Sci. USSR **8**, 451 (1934).
- [2] I. M. Frank and I. E. Tamm, C.R. Acad. Sci. USSR **14**, 109 (1937).
- [3] A. M. Hillas, Space Sci. Rev. **75**, 17 (1996), <https://doi.org/10.1007/BF00195021>.
- [4] R. Abbasi, et al., Nucl. Instr. and Meth. A **618**, 139 (2010), <https://doi.org/10.1016/j.nima.2010.03.102>.
- [5] K. Matsuoka, For the Belle II PID Group, Nucl. Instr. and Meth. A **732**, 357 (2013), <https://doi.org/10.1016/j.nima.2013.08.008>.
- [6] N. Akchurin, et al., Nucl. Instr. and Meth. A **638**, 47 (2011), <https://doi.org/10.1016/j.nima.2011.02.077>.
- [7] W. E. Spicer, Phys. Rev. **112**, 114 (1958), <https://doi.org/10.1103/PhysRev.112.114>.
- [8] C. N. Berglund and W. E. Spicer, Phys. Rev. **136**, A1030 (1964), <https://doi.org/10.1103/PhysRev.136.A1030>.
- [9] D. H. Dowell, F. K. King, R. E. Kirby, J. F. Schmerge, and J. M. Smedley, Phys. Rev. ST Accel. Beams **9**, 063502 (2006), <https://doi.org/10.1103/PhysRevSTAB.9.063502>.
- [10] K. L. Jensen, N. A. Moody, D. W. Feldman, E. J. Montgomery, and P. G. O'Shea, J. Appl. Phys. **102**, 074902 (2007), <https://doi.org/10.1063/1.2786028>.
- [11] K. L. Jensen, B. L. Jensen, E. J. Montgomery, D. W. Feldman, P. G. O'Shea, and N. Moody, J. Appl. Phys. **104**, 044907 (2008), <https://doi.org/10.1063/1.2967826>.
- [12] E. O. Kane, Phys. Rev. **127**, 131 (1962), <https://doi.org/10.1103/PhysRev.127.131>.
- [13] P. Dolizy, O. de Luca, and M.-A. Deloron, Acta Electron. **20**, 265 (1977).
- [14] S. M. Johnson, Jr., Appl. Opt. **31**, 2332 (1992), <https://doi.org/10.1364/AO.31.002332>.
- [15] T. Lang, Photocathode characterisation, Thorn EMI research report X.2818/1A (1993).
- [16] M. E. Moorhead and N. W. Tanner, Nucl. Instr. and Meth. A **378**, 162 (1996), [https://doi.org/10.1016/0168-9002\(96\)00447-0](https://doi.org/10.1016/0168-9002(96)00447-0).
- [17] M. D. Lay, Nucl. Instr. and Meth. A **383**, 485 (1996), [https://doi.org/10.1016/S0168-9002\(96\)00860-1](https://doi.org/10.1016/S0168-9002(96)00860-1).
- [18] M. D. Lay, Appl. Opt. **36**, 232 (1997), <https://doi.org/10.1364/AO.36.000232>.
- [19] E. Shibamura, S. Sasaki, H. Tawara, K. Saito, and M. Miyajima, Jpn. J. Appl. Phys. **45**, 5990 (2006), <https://doi.org/10.1143/JJAP.45.5990>.
- [20] C. Ghosh, Phys. Rev. B **22**, 1972 (1980), <https://doi.org/10.1103/PhysRevB.22.1972>.
- [21] S. Hallensleben, S. W. Harmer, and P. D. Townsend, Opt. Comm. **180**, 89 (2000), [https://doi.org/10.1016/S0030-4018\(00\)00694-5](https://doi.org/10.1016/S0030-4018(00)00694-5).
- [22] D. Motta and S. Schönert, Nucl. Instr. and Meth. A **539**, 217 (2005), <https://doi.org/10.1016/j.nima.2004.10.009>.
- [23] S. W. Harmer, R. Downey, Y. Wang, and P. D. Townsend, Nucl. Instr. and Meth. A **564**, 439 (2006), <https://doi.org/10.1016/j.nima.2006.04.050>.
- [24] D. P. Jones, Appl. Opt. **15**, 910 (1976), <https://doi.org/10.1364/AO.15.000910>.

-
- [25] T. H. Chyba and L. Mandel, *J. Opt. Soc. Am. B* **5**, 1305 (1988), <https://doi.org/10.1364/JOSAB.5.001305>.
- [26] K. Matsuoka, et al., *PoS(PhotoDet2015)028* (2015).
- [27] O. Deparis, *Opt. Lett.* **36**, 3960 (2011), <https://doi.org/10.1364/OL.36.003960>.
- [28] H. A. Lorentz, *Versuch einer Theorie der electrischen und optischen Erscheinungen in bewegten Körpern*, (E. J. Brill, 1895) [in German].
- [29] P. Drude, *Ann. der Physik* **306**, 566 (1900) [in German], <https://doi.org/10.1002/andp.19003060312>.
- [30] P. Drude, *Ann. der Physik* **308**, 369 (1900) [in German], <https://doi.org/10.1002/andp.19003081102>.
- [31] HORIBA Technical Note, Spectroscopic Ellipsometry, TN09 (2006) (available at: http://www.horiba.com/fileadmin/uploads/Scientific/Downloads/OpticalSchool-CN/TN/ellipsometer/Drude_Dispersion_Model.pdf, date last accessed June 18, 2018).
- [32] W. Sellmeier, *Ann. der Physik* **219**, 272 (1871) [in German], <https://doi.org/10.1002/andp.18712190612>.
- [33] *Quartz Glass for Optics Data and Properties* (Heraeus, Germany) (available at: https://www.heraeus.com/media/media/hqs/doc_hqs/products_and_solutions_8/optics/Data_and_Properties_Optics_fused_silica_EN.pdf, date last accessed June 18, 2018).
- [34] W. E. Spicer, *J. Appl. Phys.* **31**, 2077 (1960), <https://doi.org/10.1063/1.1735505>.
- [35] A. H. Sommer and W. E. Spicer, in *Photoelectronic Materials and Devices*, edited by S. Larach (Van Nostrand, Princeton, 1965).
- [36] W. E. Spicer, *J. Phys. Chem. Solids* **22**, 365 (1961), [https://doi.org/10.1016/0022-3697\(61\)90283-9](https://doi.org/10.1016/0022-3697(61)90283-9).
- [37] W. E. Spicer and A. Herrera-Gómez, SLAC-PUB-6306 (1993).
- [38] A. R. H. F. Ettema and R. A. de Groot, *Phys. Rev. B* **61**, 10035 (2000), <https://doi.org/10.1103/PhysRevB.61.10035>.
- [39] G. Murtaza, et al., *Bull. Mater. Sci.*, **39**, 1581 (2016), <https://doi.org/10.1007/s12034-016-1300-1>.
- [40] L. Galán, E. Elizalde, and E. Martinez, *Phys. Rev. B* **37**, 4225 (1988), <https://doi.org/10.1103/PhysRevB.37.4225>.
- [41] P. Dolizy, F. Grolière and M. Lemonier, *Adv. Electron. Electron Phys.* **74**, 331 (1988), [https://doi.org/10.1016/S0065-2539\(08\)60471-0](https://doi.org/10.1016/S0065-2539(08)60471-0).
- [42] L. Chen, et al., *Nucl. Instr. and Meth. A* **827**, 124 (2016), <https://doi.org/10.1016/j.nima.2016.04.100>.
- [43] S. Harmer, S. Hallensleben, and P. D. Townsend, *Nucl. Instr. and Meth. B* **166-167**, 798 (2000), [https://doi.org/10.1016/S0168-583X\(99\)01216-1](https://doi.org/10.1016/S0168-583X(99)01216-1).
- [44] P. D. Townsend, R. Downey, S. W. Harmer, Y. Wang, A. Cormack, R. Mcalpine, and T. Bauer, *J. Phys. D: Appl. Phys.* **39**, 1525 (2006), <https://doi.org/10.1088/0022-3727/39/8/012>.
- [45] R. Holtom, G. P. Hopkins and P. M. Gundry, *J. Phys. D: Appl. Phys.* **12**, 1169 (1979), <https://doi.org/10.1088/0022-3727/12/7/021>.
- [46] R. Smoluchowski, *Phys. Rev.* **60**, 661 (1941), <https://doi.org/10.1103/PhysRev.60.661>.
- [47] E. P. Gyftopoulos and J. D. Levine, *J. Appl. Phys.* **33**, 67 (1962), <https://doi.org/10.1063/1.1728530>.
- [48] Z. Ding, et al., *Proceedings of ERL2015*, 27 (2015).